

# Comparison of WindSat Brightness Temperatures With Two-Scale Model Predictions

David R. Lyzenga

**Abstract**—Predictions of the polarized microwave brightness temperatures over the ocean are made using a two-scale surface bidirectional reflectance model combined with an atmospheric radiative transfer model. The reflected atmospheric radiation is found to contribute significantly to the magnitude and directional dependence of the brightness temperatures. The predicted brightness temperatures are also sensitive to the form of the shortwave spectrum. Calculations are made using a new physically based model for the wave spectrum, and preliminary comparisons are made with WindSat observations at 10.7, 18.7, and 37 GHz, for wind speeds ranging from 0–20 m/s and for vertically integrated atmospheric water vapor concentrations from 0–70 mm. Predictions of the mean (azimuthally averaged) brightness temperatures for vertical and horizontal polarization agree quite well with WindSat observations over this range of wind speeds and water vapor concentrations. The predicted azimuthal variations of the third and fourth Stokes parameters also agree fairly well with the observations, except for the fourth Stokes parameter at 37 GHz. Further adjustments of the wave spectrum are expected to improve the agreement.

**Index Terms**—Atmospheric propagation, electromagnetic scattering, microwave radiometry, remote sensing.

## I. INTRODUCTION

THE WindSat polarimetric microwave radiometer [1] has provided a wealth of information on the polarization properties of the radiation emitted from the ocean surface and the atmosphere. The relationships between the polarimetric brightness temperatures and various geophysical parameters can be investigated empirically, through correlations with concurrent *in situ* measurements and/or meteorological analyses. However, it is also useful to understand these relationships in terms of physically based models. Such models can provide insight into the dependence of the brightness temperatures on variables that are highly correlated in nature, such as the sea surface temperature and the atmospheric water vapor. They can also assist in extrapolating the information gained from WindSat to other instruments with different operating parameters, such as the NPOESS Conically Scanning Microwave Imager and Sounder (CMIS) planned for launch in 2009.

This paper aims to contribute to a better understanding of the microwave radiation emitted from the ocean surface and the atmosphere, by comparing WindSat observations with predictions using a two-scale surface bidirectional reflectance model

Manuscript received January 31, 2005; revised July 31, 2005. This work was supported in part by the U.S. Department of the Navy under Grant N00173-04-1-G001.

The author is with the Department of Naval Architecture and Marine Engineering, University of Michigan, Ann Arbor, MI 48109-2145 USA (e-mail: lyzenga@umich.edu).

Digital Object Identifier 10.1109/TGRS.2005.857082

combined with an atmospheric radiative transfer calculation. An overview of the combined surface/atmospheric model is presented in Section II, followed by detailed descriptions of the two main components of the model in Sections III and IV. The model input parameters, including the wave spectrum, are discussed in Section V and preliminary comparisons with WindSat data are presented in Section VI. The conclusions drawn from these comparisons are summarized in the final section.

## II. MODEL OVERVIEW

The microwave radiation measured by a spaceborne radiometer includes contributions from both the Earth's surface and the atmosphere. The intensity of this radiation is usually expressed in terms of the brightness temperature, which is defined as the temperature of a black body producing the same radiant intensity, i.e.,

$$T_b = \frac{\lambda^2}{2k_B} L_\nu \quad (1)$$

where  $\lambda$  is the wavelength of the radiation,  $k_B = 1.38 \times 10^{-23}$  J·K<sup>-1</sup> is Boltzmann's constant, and  $L_\nu$  is the specific radiant intensity, in units of power per unit area per steradian and per unit bandwidth (e.g., W·m<sup>-2</sup>·sr<sup>-1</sup>·Hz<sup>-1</sup>). The polarization properties of the radiation can be described in terms of the four-component modified Stokes vector

$$\begin{aligned} \mathbf{T}_b &= [T_v, T_h, U, V] \\ &= \kappa [\langle E_v E_v^* \rangle, \langle E_h E_h^* \rangle, 2\text{Re}\langle E_v E_h^* \rangle, 2\text{Im}\langle E_v E_h^* \rangle] \end{aligned} \quad (2)$$

where  $E_v$  and  $E_h$  are the components of the electric field in the vertical and horizontal directions, respectively, and  $\kappa$  is a constant which depends on the system of units used for the electric field. The brightness temperature vector for a black body is  $\mathbf{T}_b = \boldsymbol{\epsilon}_b T$  where  $T$  is the physical temperature and  $\boldsymbol{\epsilon}_b = [1, 1, 0, 0]$  is the (unpolarized) black-body emissivity. The radiation emitted from the atmosphere is also unpolarized and can be represented by  $\mathbf{T}_b = \boldsymbol{\epsilon}_b T_u(\mu)$  in the upward hemisphere, where  $T_u(\mu)$  is the upwelling atmospheric brightness temperature and  $\mu$  is the cosine of the angle ( $\theta$ ) between the propagation direction and the positive  $z$  axis (upward direction). The radiation in the downward hemisphere is written as  $\mathbf{T}_b = \boldsymbol{\epsilon}_b T_d(\mu_i)$  where  $T_d(\mu_i)$  is the downwelling atmospheric brightness temperature and  $\mu_i$  is the cosine of the angle ( $\theta_i$ ) between the propagation direction and the negative  $z$  axis (downward direction). The radiation emitted from the surface may be polarized if the surface geometry is anisotropic (for the ocean surface this anisotropy is due to surface waves that are generated preferentially in the direction of the wind). Thus, the brightness temperature of the emitted radiation can be written as  $\mathbf{T}_b = \boldsymbol{\epsilon}_s T_s$  where  $T_s$  is

the surface temperature and  $\boldsymbol{\epsilon}_s$  is the surface emissivity vector. From Kirchhoff's law, the surface emissivity can be written as

$$\boldsymbol{\epsilon}_s(\mu, \phi) = \boldsymbol{\epsilon}_b - \int_0^1 \int_0^{2\pi} \boldsymbol{\rho}(\mu, \phi; \mu_i, \phi_i) d\mu_i d\phi_i \quad (3)$$

where  $\boldsymbol{\rho}(\mu, \phi; \mu_i, \phi_i)$  is the bidirectional reflectance vector, and  $\phi$  and  $\phi_i$  represent the azimuth angles of the reflected and incident radiation, respectively. The bidirectional reflectance vector is defined such that the reflected radiance for an unpolarized incident radiance field  $L_i(\mu_i, \phi_i)$  is given by

$$L_r(\mu, \phi) = \int_0^1 \int_0^{2\pi} \boldsymbol{\rho}(\mu, \phi; \mu_i, \phi_i) L_i(\mu_i, \phi_i) d\mu_i d\phi_i. \quad (4)$$

The brightness temperature as observed at any location above the surface consists of three components: 1) the radiation emitted from the atmosphere in the upward direction; 2) the radiation emitted from the atmosphere in the downward direction and reflected from the surface; and 3) the radiation emitted from the surface. The second two components are also reduced by losses in transmission through the atmosphere, as represented by the transmittance  $\tau(\mu)$ . Thus, the total observed brightness temperature can be written as

$$\begin{aligned} T_b(\mu, \phi) = \tau(\mu) \int_0^1 \int_0^{2\pi} \boldsymbol{\rho}(\mu, \phi; \mu_i, \phi_i) [T_d(\mu_i) - T_s] d\mu_i d\phi_i \\ + \boldsymbol{\epsilon}_b [T_u(\mu) + \tau(\mu) T_s]. \end{aligned} \quad (5)$$

The calculation of the surface bidirectional reflectance is discussed in the following section, and the calculation of the atmospheric brightness temperature and the transmittance is discussed in Section IV.

### III. SURFACE REFLECTANCE MODEL

The earliest models for the microwave emissivity of the ocean surface were based on the physical optics or Kirchhoff approximation [2]. Surface foam effects were subsequently included in order to improve predictions of the wind speed dependence [3] and the angular dependence [4] of the brightness temperatures. Direct observations indicate that foam-covered surfaces have a higher emissivity than foam-free surfaces [5], [6]; however, the wind speed dependence of the foam coverage [7] is much stronger than that of the brightness temperature. Corrections due to small-scale surface roughness effects have been incorporated using the two-scale model [8]–[11] and the small-slope approximation [12]–[16]. These two approximations are derived differently but appear to produce generally similar results. The present paper follows the two-scale approach, and differs from previous work primarily in the inclusion of atmospheric effects, which has required a reformulation of the two-scale model in terms of the bidirectional reflectance as discussed in the previous section and the following paragraphs.

In the two-scale model the ocean surface is considered as a set of facets, with the reflectance of each facet being given by the small-perturbation method (SPM) as discussed in Appendix A.

To calculate this reflectance, we define a local  $(\mathbf{x}', \mathbf{y}', \mathbf{z}')$  coordinate system for each facet, such that  $\mathbf{z}'$  axis is aligned with the local surface normal  $\mathbf{n}$ . This coordinate system can be defined as a rotation of the global  $(\mathbf{x}, \mathbf{y}, \mathbf{z})$  coordinate system through the angle  $\theta_n = \cos^{-1}(\mathbf{n} \cdot \mathbf{z})$  about the direction  $= \mathbf{n} \times \mathbf{z}$ . Applying this transformation to the other coordinate axes yields

$$\mathbf{x}' = \mathbf{x} - n_x(\mathbf{n} + \mathbf{z}) / (1 + n_z) \quad (6)$$

$$\mathbf{y}' = \mathbf{y} - n_y(\mathbf{n} + \mathbf{z}) / (1 + n_z). \quad (7)$$

The components of the scattered wavenumber vector  $\mathbf{k}$  in the local coordinate system are then given by

$$k'_x = \mathbf{k} \cdot \mathbf{x}' = k_x - n_x(k_n + k_z) / (1 + n_z) \quad (8)$$

$$k'_y = \mathbf{k} \cdot \mathbf{y}' = k_y - n_y(k_n + k_z) / (1 + n_z) \quad (9)$$

$$k'_z = \mathbf{k} \cdot \mathbf{z}' = \mathbf{k} \cdot \mathbf{n} = k_n = k \cos \theta' \quad (10)$$

where  $(k_x, k_y, k_z)$  are the components of  $\mathbf{k}$  in the global coordinate system and  $k$  is the magnitude of  $\mathbf{k}$ . Similarly, the components of the incident wavenumber vector  $\mathbf{k}_i$  in the local coordinate system are given by

$$k'_{ix} = \mathbf{k}_i \cdot \mathbf{x}' = k_{ix} - n_x(k_{in} + k_{iz}) / (1 + n_z) \quad (11)$$

$$k'_{iy} = \mathbf{k}_i \cdot \mathbf{y}' = k_{iy} - n_y(k_{in} + k_{iz}) / (1 + n_z) \quad (12)$$

$$k'_{iz} = \mathbf{k}_i \cdot \mathbf{z}' = \mathbf{k}_i \cdot \mathbf{n} = k_{in} = -k \cos \theta'_i. \quad (13)$$

Equations (10) and (13) can be used to obtain the local scattering angle  $\theta'$  and incidence angle  $\theta'_i$  for a given  $\mathbf{k}_i, \mathbf{k}$ , and  $\mathbf{n}$ . These angles are used in place of  $\theta$  and  $\theta_i$ , and the components  $(k'_x, k'_y, k'_z)$  and  $(k'_{ix}, k'_{iy}, k'_{iz})$  are substituted for their counterparts in (A1)–(A12) to compute the bidirectional reflectance of the surface facet under consideration.

The components of the bidirectional reflectance vector given by (A1)–(A12) correspond to the polarization basis vectors  $(\mathbf{h}'$  and  $\mathbf{v}')$  in the local coordinate system. To compute the Stokes components in the global coordinate system, the local components must be projected onto the global basis vectors  $(\mathbf{h}$  and  $\mathbf{v})$  as described in Appendix B. These components are given by

$$\rho_v(\mu, \phi; \mu_i, \phi_i; \mathbf{n}) = \rho'_v \cos^2 \alpha + \rho'_h \sin^2 \alpha - \rho'_U \sin \alpha \cos \alpha \quad (14)$$

$$\rho_h(\mu, \phi; \mu_i, \phi_i; \mathbf{n}) = \rho'_h \cos^2 \alpha + \rho'_v \sin^2 \alpha + \rho'_U \sin \alpha \cos \alpha \quad (15)$$

$$\rho_U(\mu, \phi; \mu_i, \phi_i; \mathbf{n}) = \rho'_U \cos 2\alpha + (\rho'_v - \rho'_h) \sin 2\alpha \quad (16)$$

$$\rho_V(\mu, \phi; \mu_i, \phi_i; \mathbf{n}) = \rho'_V \quad (17)$$

where  $\cos \alpha$  and  $\sin \alpha$  are given by (B3) and (B4), and  $\rho'_v, \rho'_h, \rho'_U$ , and  $\rho'_V$  are the components of the facet reflectivity in the local coordinate system, as calculated from (A12) using the local incidence and scattering angles. The total reflectance is then given by integrating the contributions from all possible surface slopes or normal vectors, i.e.,

$$\boldsymbol{\rho}(\mu, \phi; \mu_i, \phi_i) = \int_0^\pi \int_0^{2\pi} \boldsymbol{\rho}(\mu, \phi; \mu_i, \phi_i; \mathbf{n}) p'_n(\mathbf{n}) \sin \theta_n d\theta_n d\phi_n \quad (18)$$

where  $p'_n(\mathbf{n})$  is the modified probability density function for the surface normal, as discussed in Appendix C. In evaluating this

integral, it is also possible to incorporate the effects of correlations between the small-scale roughness and the large-scale surface slope due to hydrodynamic interactions between long-waves and shortwaves. These interactions can be described by means of the dimensionless modulation transfer function  $m = m_r + im_i$ , which is defined such that the fractional modulation of the shortwave spectral density is given by

$$f(x, y) = \text{Re} \int \int m k \psi(k_x, k_y) e^{i(k_x x + k_y y)} dk_x dk_y \quad (19)$$

where  $\psi(k_x, k_y)$  is the one-sided Fourier transform of the surface elevation and the integral is carried out over all wavenumbers over which the Fourier transform is defined. The surface slopes in the upwind and crosswind directions are given in terms of this Fourier transform by

$$\eta_u(x, y) = \text{Re} \int \int i k_u \psi(k_x, k_y) e^{i(k_x x + k_y y)} dk_x dk_y \quad (20)$$

$$\eta_c(x, y) = \text{Re} \int \int i k_c \psi(k_x, k_y) e^{i(k_x x + k_y y)} dk_x dk_y \quad (21)$$

where  $k_u = k_x \cos \phi_w + k_y \sin \phi_w$ ,  $k_c = k_y \cos \phi_w - k_x \sin \phi_w$ , and  $\phi_w$  is the wind direction relative to the  $x$  axis. Using the properties  $\langle \psi(k_x, k_y) \psi(k'_x, k'_y) \rangle = 0$  and

$$\langle \psi(k_x, k_y) \psi^*(k'_x, k'_y) \rangle = 2S(k_x, k_y) \delta(k_x - k'_x) \delta(k_y - k'_y) \quad (22)$$

where  $S(k_x, k_y)$  is the one-sided wave height spectrum, the correlations between the shortwave spectral density and the surface slopes are then given by

$$\langle f \eta_u \rangle = \int \int m_i k k_u S(k_x, k_y) dk_x dk_y \quad \langle f \eta_c \rangle = 0. \quad (23)$$

The predicted or expected value of the fractional spectral modulation is therefore proportional to the upwind surface slope, i.e.,  $\hat{f} = m' \eta_u$  where

$$m' = \frac{\langle f \eta_u \rangle}{\langle \eta_u^2 \rangle} = \frac{\int \int m_i k k_u S(k_x, k_y) dk_x dk_y}{\int \int k_u^2 S(k_x, k_y) dk_x dk_y}. \quad (24)$$

This effect is incorporated into the two-scale model by multiplying the SPM contributions to the reflectivity of each facet by the factor  $1 + m' \eta_u$ .

The integrand in (18) can be broken into its coherent and incoherent components as described in Appendix A. The coherent component can be evaluated analytically to yield the result

$$\rho_c(\mu, \phi; \mu_i, \phi_i) = \frac{1}{4\mu'_s} \mathbf{R}_c(\mu'_s, \mathbf{n}_s) \mathbf{p}'_n(\mathbf{n}_s) \quad (25)$$

where  $\mathbf{n}_s = (\mathbf{k} - \mathbf{k}_i)/2\mu'_s$  is the specular surface normal for the look direction  $\mathbf{k}$  and the incident direction  $\mathbf{k}_i$ , and

$$\mathbf{R}_c(\mu'_s, \mathbf{n}_s) = \mathbf{R}(\mu'_s, \mathbf{n}_s) + \delta \mathbf{R}(\mu'_s, \mathbf{n}_s) [1 + m' \eta_u] \quad (26)$$

where  $\mathbf{R}(\mu', \mathbf{n})$  is the geometric-optics reflectivity and  $\delta \mathbf{R}(\mu', \mathbf{n})$  is the second-order SPM correction vector discussed in Appendix A, evaluated at the local incidence angle and projected onto the global polarization basis vectors as described in (14)–(17). The procedure for computing this component is to first choose an observation direction  $(\mu, \phi)$

and then loop over a set of incidence directions  $(\mu_i, \phi_i)$ . For each incidence direction, the specular surface normal  $\mathbf{n}_s$  and the cosine  $\mu'_s$  of the local incidence angle is calculated, and (25) is evaluated. Note that this procedure is guaranteed to produce a valid surface normal for each incidence direction, but it does not automatically include multiple reflections. Thus, the procedure up to this point would imply the use of “Stogryn shadowing” [16]. To explicitly include multiple scattering, we reverse the sign of  $\mu_i$  and repeat the procedure, and add the two contributions together. This procedure is tantamount to assuming that during the previous interaction the surface was flat, horizontal, and a perfect reflector. This assumption is also implicitly made when the emissivity is calculated by simply integrating the bidirectional reflectance over all slopes and all incidence angles, as in [9], without any special treatment of the slopes for which  $\mu_i > 0$  or  $k_z > 2\mu' n_z$ .

The incoherent component of the bidirectional reflectance is computed by numerically integrating (18) using the first-order SPM reflectivity discussed in Appendix A, again evaluated at the local incidence angle and projected onto the global polarization basis vectors, and multiplied by the factor  $[1 + m' \eta_u]$  to account for hydrodynamic modulation effects. This integration is carried out over polar angles  $(\theta_n)$  from zero to a maximum angle corresponding to five times the rms surface slope, and over all azimuthal angles  $(\phi_n)$ .

The incidence directions are selected to sample the angular variation of the bidirectional reflectance as efficiently as possible. The zenith angles  $(\theta_i)$  are uniformly sampled, while the azimuthal angles  $(\phi_i)$  are sampled more finely as the zenith angle increases, so as to produce directional samples with roughly equal solid angles. Specifically, the number of azimuthal samples is equal to  $n_a = 4(2i_p - 1)$  where  $i_p = 1, \dots, n_p$  is the zenith angle sample number. The total number of incidence direction samples using this procedure is  $n_t = 4n_p^2$ . Since most applications involve an integration over azimuthal angles, the quantity

$$\bar{\rho}(\mu, \phi; \mu_i) = \int_0^{2\pi} \rho(\mu, \phi; \mu_i, \phi_i) d\phi_i \quad (27)$$

is then computed and stored for later use. Frequently, as in the case of a conically scanning radiometer, the nadir angle  $(\theta)$  is fixed but the look direction  $(\phi)$  is variable, so the calculation is repeated for a series of look directions.

Surface foam effects could also be incorporated into this model, although they have not yet been included. One possible approach would be to incorporate these effects by modifying the effective dielectric constant of the surface. The effective dielectric constant could then be used directly in the reflectivity model described above, in order to evaluate the effects of foam on all four of the Stokes parameters.

#### IV. ATMOSPHERIC MODEL

At microwave frequencies, atmospheric scattering can be neglected for the cases of interest where there is little or no precipitation. The radiative transfer equation then reduces to

$$\frac{dT_b}{ds} = \alpha(s)[T(s) - T_b(s)] \quad (28)$$

where  $s$  is the distance along a straight-line path through the atmosphere,  $\alpha$  is the absorption coefficient,  $T$  is the physical temperature of the atmosphere, and  $T_b$  is the brightness temperature for a look direction along the path. This equation can be readily integrated to yield

$$T_d(\mu) = \int_0^{\infty} \alpha(z)T(z)\tau(0, z)ds \quad (29)$$

for the downwelling brightness temperature at the surface ( $s = 0$  or  $z = 0$ ) and

$$T_u(\mu) = \int_0^S \alpha(z)T(z)\tau(z, z_s)ds \quad (30)$$

for the upwelling brightness temperature at the sensor ( $s = S$  or  $z = z_s$ ), where  $z$  is the altitude above the surface and

$$\tau(z_1, z_2) = \exp \left\{ - \int_{z_1}^{z_2} \alpha(z)ds \right\} \quad (31)$$

is the transmittance along the path from  $z_1$  to  $z_2$ . For a spherical Earth atmosphere the path length is related to the altitude through the equation

$$s = \sqrt{(R_e + z)^2 - R_e^2 \sin^2 \theta} - R_e \cos \theta \quad (32)$$

where  $R_e$  is the Earth's radius, while for a plane-parallel atmosphere  $s = z \sec \theta = z/\mu$ . Note that the atmospheric radiation is unpolarized, so the horizontally and vertically polarized brightness temperatures are equal, and the third and fourth Stokes parameters are zero. The cosmic background radiation is included in the downwelling brightness temperature by adding the term  $\tau(0, \infty) T_{bc}$  to (29), where  $T_{bc} = 2.7$  K.

Evaluation of (29) and (30) requires a knowledge of the atmospheric temperature and the absorption coefficient as a function of the altitude. The absorption coefficient is calculated using the models for oxygen, water vapor, and cloud liquid water published by Liebe *et al.* [17]. The model for oxygen includes a set of 37 absorption lines centered at frequencies ranging from about 50–70 GHz, and several additional lines above 100 GHz, plus a nonresonant continuum term. The line strengths and line shapes and the continuum term are all functions of the atmospheric pressure and temperature. The water vapor model includes a strong absorption line near 22 GHz, a much weaker line near 68 GHz, and 32 lines above 100 GHz plus a continuum term, all of which are functions of the water vapor pressure as well as the total atmospheric pressure and temperature. The liquid water absorption is calculated from the Rayleigh approximation for the particle extinction, using a double-Debye model for the complex permittivity of water. The total absorption coefficient is proportional to the amount of liquid water (in grams per cubic meter of air) and is also dependent on the cloud temperature, because of the temperature dependence of the permittivity.

To calculate the absorption coefficient as a function of the altitude we need to specify the temperature and pressure of the air, as well as the water vapor and liquid water concentrations. The temperature profile is also used directly in (29) and (30).

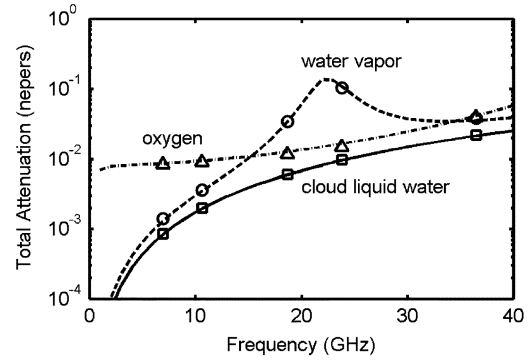


Fig. 1. Vertically integrated attenuation coefficients for oxygen, water vapor, and cloud liquid water for a total water vapor content of 20 mm and a cloud liquid water content of 0.1 mm. Symbols indicate values from Wentz and Meissner [19] for the AMSR frequencies.

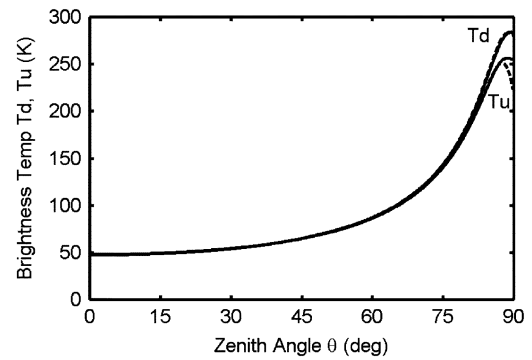


Fig. 2. Upwelling and downwelling atmospheric brightness temperatures as functions of the zenith angle, for a total water vapor content of 20 mm and no cloud liquid water, with a surface temperature of 285 K. Solid curves are for a spherical Earth atmosphere, and dashed curves are for a plane-parallel atmosphere.

For the purposes of these calculations we use the 1976 Standard Atmosphere for the temperature and pressure profiles and assume a constant relative humidity versus altitude. The cloud liquid water is assumed to be concentrated at a single altitude, and to have the temperature of the air at that altitude. The 1976 Standard Atmosphere consists of seven layers, with a temperature lapse rate of 6.5 K/km in the lowest (0–11 km) layer. The pressure is calculated from the hydrostatic equations using the ideal gas law for the density of air. The water vapor pressure is calculated by multiplying the relative humidity by the saturation vapor pressure, which is a function of the temperature [18]. Examples of the vertically integrated attenuation coefficients for oxygen, water vapor, and cloud liquid water are shown as functions of the frequency in Fig. 1.

Using the sum of the attenuation coefficients for these three constituents for  $\alpha(z)$  and the temperature profile from the 1976 Standard Atmosphere for  $T(z)$ , (29) and (30) were evaluated numerically for both the spherical Earth and the plane-parallel atmosphere cases. Example results for the upwelling and downwelling brightness temperatures are shown in Fig. 2 as functions of the zenith angle  $\theta$ . Note that the upwelling and downwelling brightness temperatures are nearly equal for zenith angles less than about 75°, and the results for the spherical Earth case differ from the plane-parallel case hardly at all for downwelling radiation and only at zenith angles greater than 85° for upwelling radiation.

## V. MODEL INPUT PARAMETERS

Evaluation of the surface reflectance model requires a specification of several physical parameters including the sea water dielectric constant, the surface slope probability density function, the wave height spectrum, and the hydrodynamic modulation transfer function. For the sea water dielectric constant, we have used the model of Ellison *et al.* [20]. The surface slope probability density function is assumed to be Gaussian, i.e.,

$$p(\eta_u, \eta_c) = \frac{1}{2\pi\sigma_u\sigma_c} \exp\left\{-\frac{1}{2}[(\eta_u/\sigma_u)^2 + (\eta_c/\sigma_c)^2]\right\} \quad (33)$$

with slope variances

$$\sigma_u^2 = \int_0^{k_c} \int_{-\pi}^{\pi} k^2 \cos^2(\phi - \phi_w) S(k, \phi) dk d\phi \quad (34)$$

$$\sigma_c^2 = \int_0^{k_c} \int_{-\pi}^{\pi} k^2 \sin^2(\phi - \phi_w) S(k, \phi) dk d\phi \quad (35)$$

where  $S(k, \phi)$  is the wave height spectrum (see below),  $k_c = 0.3k_o$ , and  $\phi_w$  is the wind direction. The probability density function can also be expressed in terms of the  $x$ - $y$  components of the slope ( $\eta_x$  and  $\eta_y$ ) by substituting  $\eta_u = \eta_x \cos \phi_w + \eta_y \sin \phi_w$  and  $\eta_c = \eta_y \cos \phi_w - \eta_x \sin \phi_w$  in (33).

It is possible to modify (33) to allow for asymmetries in the slope distribution, as in Cox and Munk [21], in order to account for upwind/downwind differences in the brightness temperatures. However, we have chosen to account for these differences by means of the modulation transfer function discussed in Section III. Models and measurements of the modulation transfer function exist [22] but there is a large variability in the imaginary part of this transfer function. Values for  $m_i$  have also been inferred by fitting two-scale model predictions to measurements of the radar cross section [23]. The modulation transfer function used by Yueh [9] can be written in our notation as

$$m' = \begin{cases} -0.4/\sigma_u, & \text{for } |\eta_u| \leq 1.25\sigma_u \\ -0.5/|\eta_u|, & \text{for } |\eta_u| > 1.25\sigma_u \end{cases} \quad (36)$$

where  $m'$  is the quantity defined in (24),  $\sigma_u^2$  is the upwind slope variance, and  $\eta_u$  is the upwind slope as defined in (20). This formulation produces a maximum fractional modulation of  $\pm 0.5$ , or a small-scale roughness that is at most three times larger on the lee side than on the windward side of the long waves.

To construct a model for the wave height spectrum, we have adopted an approach based on energy balance considerations, as discussed in [23]. In that work, a form for the equilibrium spectrum was derived using two energy input terms (corresponding to a linear and an exponential growth rate) and two dissipation terms (intended to represent viscous dissipation and energy loss due to wave breaking or other nonlinear effects). The parameters in this model were adjusted to fit the C-band radar cross section measurements represented by the CMOD4 model function [24]. However, to account for observations at higher frequencies, an additional source term for capillary-gravity waves needs to be incorporated into this model, as discussed below.

The source function used in [23] can be written as

$$F_s(k, \phi) = \alpha_{\text{pm}}(k, \phi) + [\beta - 4\nu k^2]B(k, \phi) - \gamma B(k, \phi)^2 \quad (37)$$

where  $\alpha_{\text{pm}}(k, \phi)$  is the linear growth rate, often associated with the Phillips mechanism [25],  $\beta$  is the exponential growth rate,  $\nu = 0.01 \text{ cm}^2/\text{s}$  is the molecular kinematic viscosity of sea water,  $\gamma$  is a nonlinear dissipation parameter, and  $B(k, \phi)$  is the curvature spectrum, defined as  $k^4$  times the height spectrum  $S(k, \phi)$ . Solving the equation  $F_s(k, \phi) = 0$  yields the equilibrium spectrum

$$B(k, \phi) = B_o(k, \phi) + \sqrt{B_o^2(k, \phi) + \alpha_{\text{pm}}(k, \phi)/\gamma} \quad (38)$$

where  $B_o(k, \phi) = [\beta - 4\nu k^2]/2\gamma$ . In order to make the spectrum approach the form proposed by Pierson and Moskowitz [26] at low wavenumbers, we choose

$$\alpha_{\text{pm}}(k, \phi) = \gamma S_{\text{pm}}^2(\omega) \Phi^2(\phi - \phi_w) \quad (39)$$

where  $S_{\text{pm}}(\omega)$  is the Pierson–Moskowitz frequency spectrum, which is converted into a wavenumber spectrum using the full gravity-capillary dispersion relation, and  $\Phi(\phi)$  is an angular distribution which is assumed to have the  $\cos^{2s}(\phi)$  form used by Hasselmann *et al.* [27].

The exponential growth rate in (37) is assumed to have the form

$$\beta(k, \phi) = [b_0 + b_1 \cos(\phi - \phi_w) + b_2 \cos 2(\phi - \phi_w)]k/c \quad (40)$$

where  $b_0, b_1$ , and  $b_2$  are functions of the wind speed ( $b_2$  is chosen to be equal to  $b_1 - b_0$  so that  $\beta(k, \phi_w + \pi) = 0$ ), and  $c$  is the wave phase velocity. The wavenumber dependence of  $\beta$  is approximately the same as that proposed by Plant [28]. The values of  $b_0, b_1$ , and  $b_2$  were determined in [23] by fitting predicted radar cross sections to CMOD4 values, as mentioned earlier, using  $\gamma = \gamma_o \omega$  with  $\gamma_o = 0.33$ .

To extend the spectrum to wavelengths shorter than a few centimeters, we add another source term of the form

$$\alpha_{\text{pc}}(k, \phi) = \gamma \alpha_p^2 f_p^2(k) \Phi_p^2(\phi - \phi_w) \quad (41)$$

to the right-hand side of (37), where  $\alpha_p$  and  $p$  are functions of the wind speed,

$$f_p(k) = \exp\left\{-\frac{1}{2}(k/k_c - k_c/k)^2\right\} \quad (42)$$

with  $k_c = 750 \text{ rad/m}$ , and

$$\Phi_p(\phi) = A_p \exp\{p \cos \phi\} \quad (43)$$

where  $A_p = [2\pi I_o(p)]^{-1}$  and  $I_o(p)$  is the modified Bessel function, so that the integral of  $\Phi_p(\phi)$  over all angles is equal to one. This function is very similar to the  $\cos^{2s}(\phi)$  form if  $p$  is chosen as  $p = (1 + s)/2$ , and allows for a smooth transition between a sharply peaked distribution for large  $p$  to an isotropic distribution for  $p = 0$ .

This source term is intended to represent the transfer of energy from longer to shorter waves due to nonlinear processes such as parasitic capillary wave generation and wave breaking [29], [30]. Ultimately, the amplitude of this term may be found to depend on some integral property of the spectrum at longer wavelengths. For the present, however, we assume that these processes depend only on the wind speed, and choose the parameters in (41) to produce a best fit with scatterometer as well as radiometer data. Initial estimates of these parameters produce the spectrum shown in Fig. 3. The spectral peak produced by this source term is qualitatively similar to that appearing in optical

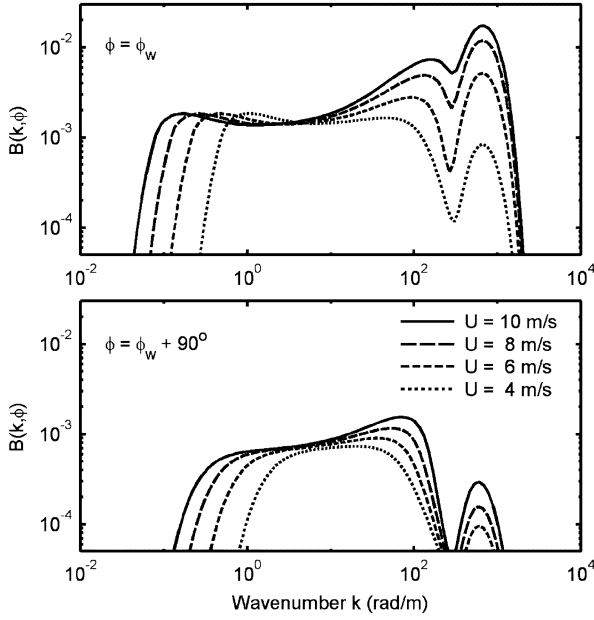


Fig. 3. Curvature spectrum in upwind and crosswind directions for four wind speeds.

measurements of the shortwave spectrum [31], [32]. Similar features have also been incorporated into wave spectrum models such as those of Apel [33], Elfouhaily *et al.* [34], Kudryavtsev *et al.* [35], and others.

In order to investigate the dependence of the polarimetric brightness temperatures on the relative azimuth angle between the look direction and the wind direction, the reflectance model is typically evaluated at 13 values of this relative azimuth angle ( $\phi$ ), from  $0^\circ$  to  $180^\circ$ . The bidirectional reflectance is first calculated over the set of incidence directions ( $\mu_i, \phi_i$ ) described in Section III, and is integrated over  $\phi_i$  as indicated in (27) to yield the quantity  $\bar{\rho}(\mu, \phi; \mu_i)$  which is stored on disk. One set of calculations for 30 incidence angles and 13 azimuth angles requires about 30 s of CPU time using a 2.8-GHz Pentium processor. The atmospheric model is then used to calculate the downwelling brightness temperature ( $T_d$ ) for the same set of incidence angles, as well as the upwelling brightness temperature ( $T_u$ ) and transmittance ( $\tau$ ) for the nadir angle  $\theta = \cos^{-1}(\mu)$ . The total brightness temperature is then calculated as

$$\mathbf{T}_b(\mu, \phi) = \tau(\mu) \int_0^1 \bar{\rho}(\mu, \phi; \mu_i) [T_d(\mu_i) - T_s] d\mu_i + \epsilon_b [T_u(\mu) + \tau(\mu) T_s] \quad (44)$$

for each of the relative azimuth angles ( $\phi$ ). The even Fourier harmonic coefficients are then calculated for the first two Stokes parameters using

$$a_n = \frac{1}{2\pi} \int_0^{2\pi} T_b(\mu, \phi) \cos(n\phi) d\phi \quad (45)$$

for  $n = 0, 1$ , and 2, and the odd harmonics are calculated for the third and fourth Stokes parameters using

$$b_n = \frac{1}{2\pi} \int_0^{2\pi} T_b(\mu, \phi) \sin(n\phi) d\phi \quad (46)$$

for  $n = 1$  and 2. The effects of atmospheric variations can be investigated with very little additional expense by repeating the process using the same set of bidirectional reflectance values, since the atmospheric model requires much less computing time than the reflectance model.

## VI. COMPARISONS WITH WINDSAT DATA

Some preliminary comparisons have been made between this model and a set of WindSat observations collected over the three-month period from September through November, 2003. The entire dataset distributed by the Naval Research Laboratory for this time period was used, including both fore and aft scans. That is, no additional editing of the data was done, other than removing points flagged as land or ice. The September datasets were from the SDR release 1.61 and the remaining datasets were from the 1.81 release (as downloaded from the JPL PODAAC web site during February 2005). The WindSat brightness temperatures were binned by the total columnar water vapor ( $wv$ ), the surface wind speed ( $U_w$ ), and the relative look direction ( $\phi - \phi_w$ ), using outputs from the NOAA Global Data Assimilation System, or GDAS [36], which were registered spatially and temporally with the WindSat data and distributed with this data on the JPL PODAAC web site. Other GDAS variables used in this study included the cloud liquid water ( $clw$ ) and the sea surface temperature ( $T_s$ ). Because of the rapid spatial and temporal variations of the cloud liquid water [37], however, these values are not well correlated with WindSat data and therefore were not considered to be useful for point-by-point comparisons with this data. Instead, the average liquid water content and surface temperature were calculated for each water vapor and wind speed bin, and these average values were used as inputs into the model, under the assumption that the actual values are uniformly distributed with respect to the relative look direction.

The bin widths used in this analysis were 10 mm in water vapor (from 0–70 mm), 2 m/s in wind speed (from 0–20 m/s), and  $15^\circ$  in relative look direction (from  $0^\circ$  to  $360^\circ$ ). The azimuthal Fourier harmonic coefficients were calculated as described in (45) and (46) using the binned brightness temperatures for each one-week period, and these weekly coefficients were averaged over the 13-week period considered in this study. The rms difference between the Fourier series fits and the individual brightness temperatures for the cases considered below is 0.59 K for  $T_v$ , 0.90 K for  $T_h$ , 0.07 K for  $U$ , and 0.02 K for  $V$ . The relatively large errors in the Fourier fits for  $T_v$  and  $T_h$  are assumed to be primarily due to variations in the cloud liquid water content, but may also reflect changes in the Earth incidence angle due to satellite attitude variations. Use of a simplified cloud liquid water estimation algorithm was found to reduce the random variability in the first two Stokes parameters. However, because of the possibility of directional leakage in the liquid water algorithm [38], there remain questions about the accuracy of the higher Fourier harmonics of  $T_v$  and  $T_h$  derived from this analysis. This paper therefore concentrates on the azimuthally averaged or zeroth harmonics of  $T_v$  and  $T_h$ , as well as the higher Fourier harmonics of  $U$  and  $V$ , which are much less affected by variations in the cloud liquid water content.

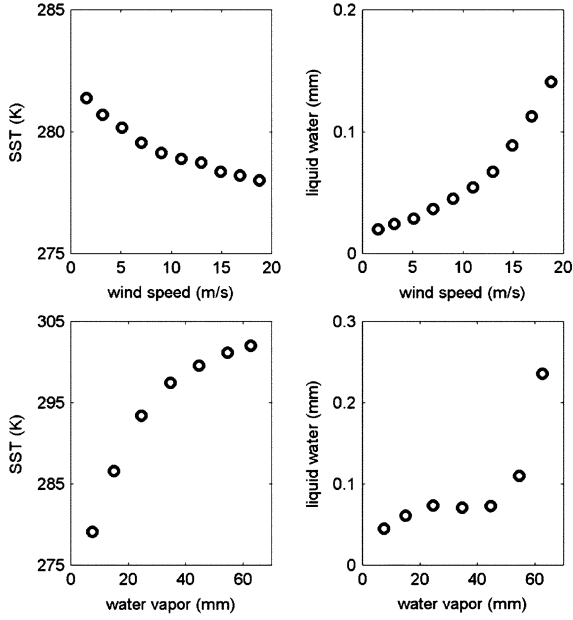


Fig. 4. Average GDAS sea surface temperature and liquid water content (upper panels) plotted versus wind speed for the lowest water vapor bin and (lower panels) the same quantities plotted versus water vapor for the 8–10 m/s wind speed bin. Values shown in the upper panels were used for the case 1 calculations, and those shown in the lower panels were used for the case 2 calculations.

Results are presented here for two cases. Case 1 deals with the variation of the brightness temperatures with wind speed for the lowest water vapor bin (0–10 mm), while case 2 examines the dependence on water vapor for an intermediate wind speed bin (8–10 m/s). In each case, the model was run using the mean values of the GDAS cloud liquid water and surface temperature for each bin, as shown in Fig. 4. In addition, to illustrate the effects of variations in the cloud liquid water, calculations were repeated for  $clw = 0$  and for values of the  $clw$  equal to twice the GDAS values shown in Fig. 4. The salinity was assumed to be 35 ppt, and nominal incidence angles of  $49.9^\circ$ ,  $55.3^\circ$ , and  $53.0^\circ$  were used for the 10.7-, 18.7-, and 37.0-GHz channels, respectively [1]. The calculations also used the wave spectrum shown in Fig. 3 and the modulation transfer function described by Yueh [9].

The calculated Fourier coefficients for case 1 are compared with the observed values in Fig. 5, and the mean and rms difference between the observations and calculations (using the GDAS  $clw$  values) are shown in Table I. The vertically polarized brightness temperatures, shown in the upper left panel of Fig. 5, have a relatively weak dependence on the wind speed, while those for horizontal polarization (upper right panel) have a much stronger wind speed dependence, consistent with previous SSM/I observations [39]. A fairly significant portion of the apparent wind speed dependence of  $T_v$  and  $T_h$  at the higher frequencies may be due to covarying changes in the cloud liquid water content, as shown in Fig. 4. The calculations agree quite well with the observations in terms of the wind speed dependence, although the calculated values of  $T_v$  are consistently below the observations by a few degrees (see Table I). Part of this discrepancy may be due to the neglect of foam, but in that case the difference would be larger for  $T_h$  than for  $T_v$ , and should be a much stronger function of the wind speed. The discrepancies may also be due to differences

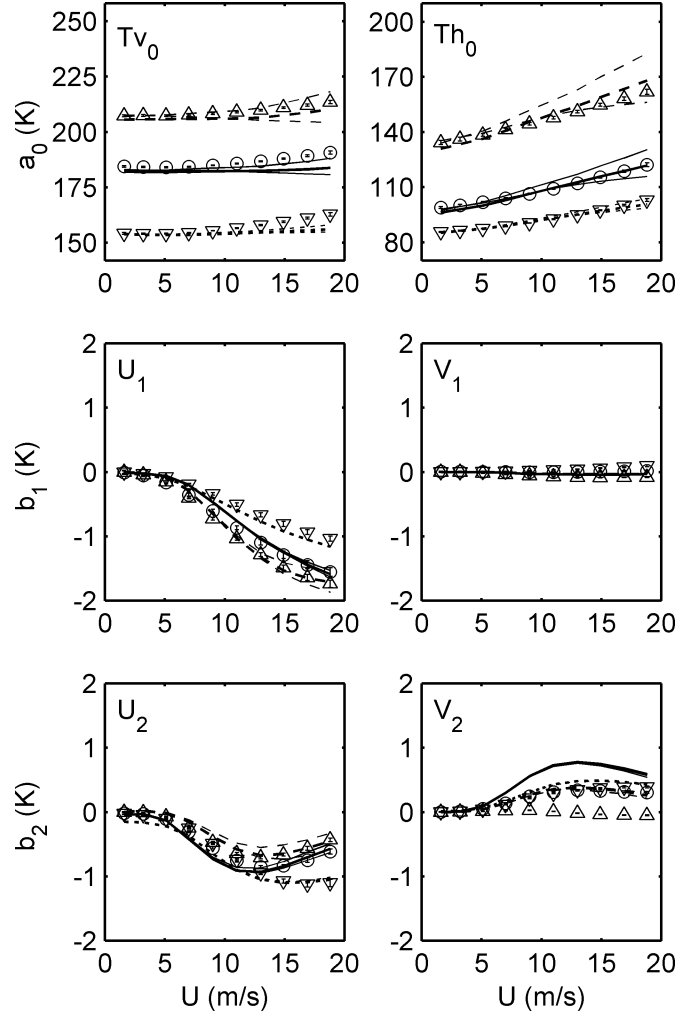


Fig. 5. Comparison of observed Fourier harmonic coefficients for  $wv = 0$ –10 mm ( $\nabla = 10.7$  GHz,  $O = 18.7$  GHz,  $\Delta = 37.0$  GHz) with predictions (dotted curves = 10.7 GHz, solid curves = 18.7 GHz, dashed curves = 37.0 GHz). Three sets of predictions are shown for (lower) no  $clw$ , (middle)  $clw$  equal to the GDAS values, and (upper curves)  $clw$  equal to twice the GDAS values.

TABLE I  
MEAN AND RMS DIFFERENCE BETWEEN OBSERVED AND CALCULATED  
AZIMUTHAL HARMONICS FOR CASE 1 (USING GDAS  $CLW$  VALUES)

parameter	10.7 GHz		18.7 GHz		37.0 GHz	
	mean	rms	mean	rms	mean	rms
$Tv_0$	2.61	3.39	3.73	4.09	2.50	2.61
$Th_0$	0.32	0.90	0.65	1.30	-1.33	3.50
$U_1$	0.07	0.08	-0.06	0.08	-0.02	0.05
$U_2$	0.08	0.11	0.05	0.09	-0.04	0.05
$V_1$	0.05	0.07	0.03	0.03	-0.03	0.04
$V_2$	-0.07	0.08	-0.24	0.30	-0.22	0.27

between the actual Earth incidence angles and the assumed nominal values. The harmonics of  $U$  and  $V$  are also fairly well predicted, with mean and rms errors less than about 0.1 K in all cases except for the second harmonic of  $V$ , which is noticeably overpredicted at 18 and 37 GHz. Better agreement of these harmonics can probably be achieved by further tuning of the surface wave spectrum and modulation transfer function, although it is not clear that such adjustments will be able to

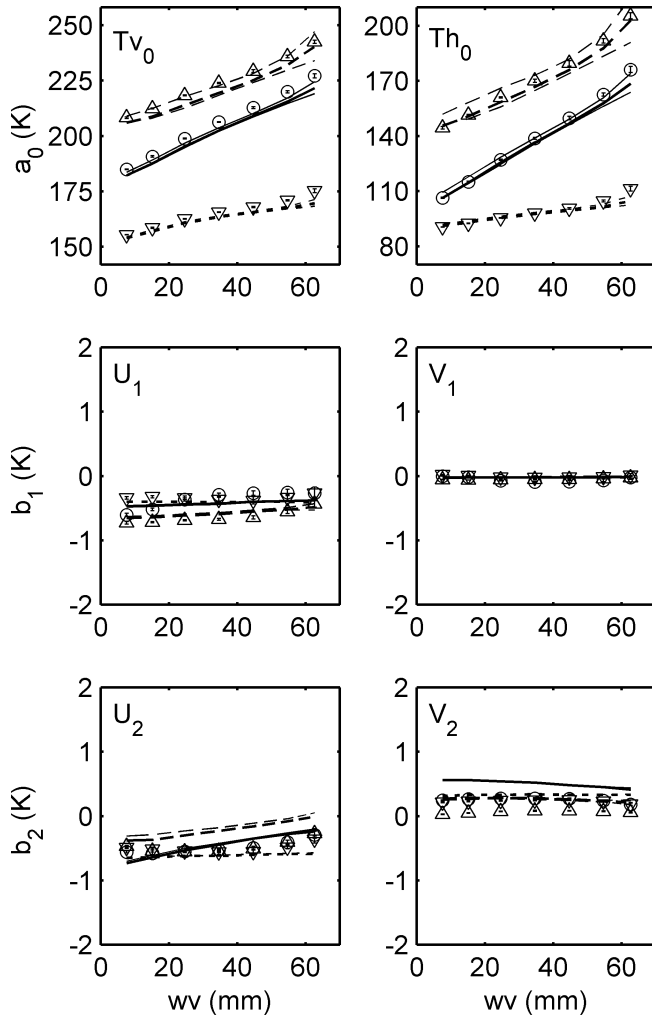


Fig. 6. Comparison of observed Fourier harmonic coefficients for  $U_w = 8-10$  m/s ( $\nabla = 10.7$  GHz,  $O = 18.7$  GHz,  $\Delta = 37.0$  GHz) with predictions (dotted curves = 10.7 GHz, solid curves = 18.7 GHz, dashed curves = 37.0 GHz). Three sets of predictions are shown for (lower) no clw, (middle) clw equal to the GDAS values, and (upper curves) clw equal to twice the GDAS values.

TABLE II  
MEAN AND RMS DIFFERENCE BETWEEN OBSERVED AND CALCULATED  
AZIMUTHAL HARMONICS FOR CASE 2 (USING GDAS CLW VALUES)

parameter	10.7 GHz		18.7 GHz		37.0 GHz	
	mean	rms	mean	rms	mean	rms
Tv0	2.68	3.00	3.84	3.94	3.51	3.62
Th0	1.48	2.79	2.76	3.70	2.21	2.75
U1	0.07	0.08	0.06	0.12	-0.06	0.07
U2	0.12	0.13	-0.03	0.11	-0.25	0.27
V1	0.02	0.02	-0.03	0.05	-0.03	0.03
V2	-0.10	0.10	-0.25	0.26	-0.20	0.20

produce the extremely small values of  $V$  that are observed at 37 GHz.

The Fourier harmonics for case 2 are plotted versus the atmospheric water vapor content in Fig. 6, and the mean and rms differences between the calculated and observed values are given in Table II. The strong dependence of  $T_v$  and  $T_h$  on the water vapor is quite well predicted over the range of

0–70 mm. The third and fourth Stokes parameters have a weaker but still significant dependence, which is fairly well predicted for the first harmonics but not as well for the second harmonics.

The predicted water vapor effects are of course dependent on the atmospheric model, but they are also influenced by the surface reflectivity in cases where the reflected downwelling radiation contributes significantly to the total brightness temperature. For the first two Stokes parameters, the reflected brightness temperature can be approximated by assuming a flat surface and multiplying the downwelling brightness temperature by the Fresnel reflectivity. For the third and fourth Stokes parameters, the reflected term in this approximation is identically zero, because the atmospheric radiation is unpolarized. A second approximation is to assume that the surface reflectivity is equal to  $\epsilon_b - \epsilon_s$  where  $\epsilon_s$  is the surface emissivity and  $\epsilon_b$  is the black-body emissivity. This approximation, which is equivalent to using the hemispherically averaged surface reflectivity, produces a nonzero result but still underestimates the magnitude of the surface-reflected term in most cases.

The surface-reflected term contributes most strongly to the zeroth harmonics of  $T_v$  and  $T_h$  and the second harmonic of  $U$  (there are also quite significant effects on the second harmonic of  $T_h$ ). Both approximations produce similar results, and can cause errors on the order of 4 K in  $T_h$  and 0.5 K in  $U$ , for large values of the water vapor content. Note that for the third and fourth Stokes parameters, the sign of the reflected term is opposite to that of the direct emission term, so an underprediction of the magnitude of the surface-reflected term causes the total brightness temperature to be overestimated.

## VII. SUMMARY AND CONCLUSION

A physically based model for the microwave brightness temperature over the ocean is described, and preliminary comparisons of the model predictions with WindSat observations are presented in this paper. Predictions of the azimuthally averaged brightness temperatures for vertical and horizontal polarization agree quite well with WindSat observations, despite the fact that foam effects have not been included. The variations of the third and fourth Stokes parameters with wind speed, water vapor, and relative look direction are also fairly well predicted, with the exception of the fourth Stokes parameter at 37 GHz. The agreement is expected to be improved by further adjustments of the wave spectrum and modulation transfer function. The higher azimuthal Fourier harmonics of  $T_v$  and  $T_h$  are not discussed in this paper because of unresolved questions about the effects of cloud liquid water on the observed values of these harmonics.

In addition to improvements in the model itself, future efforts will be directed toward more detailed comparisons with WindSat data, and utilization of the model for developing wind vector retrieval and other geophysical estimation algorithms. Model improvements will focus on adjustments of the wave spectrum and other input parameters in order to be consistent with WindSat brightness temperatures and also with radar backscatter measurements over a range of frequencies and incidence angles. Future comparisons with WindSat data will include an examination of the effects of Earth incidence angle variations, as well as better methods of accounting for cloud

liquid water and other atmospheric effects, in order to test model predictions of the higher harmonics of  $T_v$  and  $T_h$ .

Finally, the utilization of the model for the development of geophysical estimation algorithms will be explored, starting with atmospheric correction procedures. One possible atmospheric correction methodology involves an explicit estimation of atmospheric parameters followed by a removal of their effects from the measured brightness temperatures. Another possibility is to transform or combine the brightness temperatures into variables that are less sensitive to atmospheric effects, such as the combination  $2T_v - T_h$  proposed by Meissner and Wentz [38]. Adopting this approach, the next problem would then be to determine the relationship between the transformed variables and the geophysical quantities of interest, such as the wind speed and direction.

## APPENDIX A

### SPM BIDIRECTIONAL REFLECTANCE MODEL

Expressions for the surface reflectance have been derived by Yueh *et al.* [40] using the small perturbation method (SPM). This solution consists of two parts: 1) a diffuse or incoherent component and 2) a correction to the coherent (geometric optics) solution. The first component is proportional to the surface wave spectrum evaluated at a surface wavenumber that depends on the electromagnetic wavelength ( $\lambda$ ) and the incident and scattering angles. If the incident radiation is unpolarized, this component can be written in terms of the bidirectional reflectance vector defined in Section II as

$$\boldsymbol{\rho}_d(\mu, \phi; \mu_i, \phi_i) = \left[ \rho_v^{(1)}, \rho_h^{(1)}, 2\text{Re} \left\{ \rho_c^{(1)} \right\}, 2\text{Im} \left\{ \rho_c^{(1)} \right\} \right] \quad (\text{A1})$$

where

$$\rho_p^{(1)} = \mu G_p^{(1)}(k_{ix}, k_{iy}) k^4 W(k_{ix} - k_x, k_{iy} - k_y) \quad (\text{A2})$$

$$G_p^{(1)} = \left| g_{ph}^{(1)} \right|^2 + \left| g_{pv}^{(1)} \right|^2, \quad G_c^{(1)} = g_{vh}^{(1)} g_{hh}^{(1)*} + g_{vv}^{(1)} g_{hv}^{(1)*} \quad (\text{A3})$$

$$g_{vv}^{(1)} = \frac{2\mu_i(\varepsilon - 1)[\varepsilon k_r k_{ir} - \kappa_z \kappa_{iz} \cos(\phi - \phi_i)]}{(\varepsilon k_z + \kappa_z)(\varepsilon k_{iz} + \kappa_{iz})}$$

$$g_{hh}^{(1)} = \frac{2\mu_i(\varepsilon - 1)k^2 \cos(\phi - \phi_i)}{(k_z + \kappa_z)(k_{iz} + \kappa_{iz})} \quad (\text{A4})$$

$$g_{vh}^{(1)} = \frac{2\mu_i(\varepsilon - 1)k\kappa_z \sin(\phi - \phi_i)}{(k_{iz} + \kappa_{iz})(\varepsilon k_z + \kappa_z)}$$

$$g_{hv}^{(1)} = \frac{2\mu_i(\varepsilon - 1)k\kappa_{iz} \sin(\phi - \phi_i)}{(k_z + \kappa_z)(\varepsilon k_{iz} + \kappa_{iz})} \quad (\text{A5})$$

$k_x = k \sin \theta \cos \phi$ ,  $k_y = k \sin \theta \sin \phi$ ,  $k_r = k \sin \theta$ ,  $k_z = k \cos \theta$ ,  $\kappa_z = k \sqrt{\varepsilon - \sin^2 \theta}$ ,  $k_{ix} = k \sin \theta_i \cos \phi_i$ ,  $k_{iy} = k \sin \theta_i \sin \phi_i$ ,  $k_{ir} = k \sin \theta_i$ ,  $k_{iz} = k \cos \theta_i$ ,  $\kappa_{iz} = k \sqrt{\varepsilon - \sin^2 \theta_i}$ ,  $k = 2\pi/\lambda$ , and  $W(k_x, k_y) = [S(k_x, k_y) + S(-k_x, -k_y)]/2$  is the symmetrized or two-sided wave height spectrum.

For a flat, horizontal surface the geometric optics reflectivity is

$$\mathbf{R}(\mu, \mathbf{z}) = \left[ |r_v(\mu)|^2, |r_h(\mu)|^2, 0, 0 \right] \quad (\text{A6})$$

where  $r_v$  and  $r_h$  are the Fresnel reflection coefficients for vertical and horizontal polarization. The second-order SPM correction to this reflectivity, as derived by Yueh *et al.* [40], can be written as

$$\delta \mathbf{R}(\mu) = 2 \left[ \text{Re} \left\{ r_v r_{vv}^{(2)*} \right\}, \text{Re} \left\{ r_h r_{hh}^{(2)*} \right\}, \text{Re} \{ r_c \}, \text{Im} \{ r_c \} \right] \quad (\text{A7})$$

where  $r_c = r_v r_{hv}^{(2)*} + r_h^* r_{vh}^{(2)}$  and

$$r_{pq}^{(2)} = \int_{-\infty}^{\infty} \int_{-\infty}^{\infty} g_{pq}^{(2)}(k_{sx}, k_{sy}) k^2 W(k_{sx} - k_x, k_{sy} - k_y) dk_{sx} dk_{sy} \quad (\text{A8})$$

$$g_{vv}^{(2)} = \frac{2(\varepsilon - 1)k_z}{(\varepsilon k_z + \kappa_z)^2} \left\{ -\varepsilon \kappa_z + \frac{(\varepsilon - 1)\kappa_z^2}{k_{sz} + \kappa_{sz}} \right. \\ \left. + \frac{2\varepsilon k_r k_u \kappa_z}{k_{sr}^2 + k_{sz} \kappa_{sz}} - \frac{(\varepsilon - 1)(\varepsilon k_r^2 k_{sr}^2 + k_u^2 \kappa_z^2)}{(k_{sz} + \kappa_{sz})(k_{sr}^2 + k_{sz} \kappa_{sz})} \right\} \quad (\text{A9})$$

$$g_{hh}^{(2)} = \frac{2(\varepsilon - 1)k_z}{(k_z + \kappa_z)^2} \left\{ \kappa_z - \frac{(\varepsilon - 1)k^2(k_u^2 + k_{sz} \kappa_{sz})}{(k_{sz} + \kappa_{sz})(k_{sr}^2 + k_{sz} \kappa_{sz})} \right\} \quad (\text{A10})$$

$$g_{vh}^{(2)} = \frac{2(\varepsilon - 1)k_z k_v k}{(k_z + \kappa_z)(\varepsilon k_z + \kappa_z)} \\ \times \left\{ \frac{\varepsilon k_r (k_{sz} + \kappa_{sz}) - (\varepsilon - 1)\kappa_z k_u}{(k_{sz} + \kappa_{sz})(k_{sr}^2 + k_{sz} \kappa_{sz})} \right\} \quad (\text{A11})$$

$g_{hv}^{(2)} = -g_{vh}^{(2)}$ ,  $k_u = (k_x k_{sx} + k_y k_{sy})/k_r$ ,  $k_v = (k_x k_{sy} - k_y k_{sx})/k_r$ ,  $k_{sr} = \sqrt{k_{sx}^2 + k_{sy}^2}$ ,  $k_{sz} = \sqrt{k^2 - k_{sr}^2}$ ,  $k_{sx}$  and  $k_{sy}$  are variables of integration, and the other variables are as previously defined. The  $g_{pp}^{(1)}$  and  $g_{pp}^{(2)}$  coefficients defined above are equivalent to those in Yueh [9], although the notation is slightly different.

The total bidirectional reflectance can then be written as

$$\boldsymbol{\rho}(\mu, \phi; \mu_i, \phi_i) = \boldsymbol{\rho}_d(\mu, \phi; \mu_i, \phi_i) + \mathbf{R}(\mu) \delta(\mu - \mu_i) \delta(\phi - \phi_i) \quad (\text{A12})$$

where  $\boldsymbol{\rho}_d(\mu, \phi; \mu_i, \phi_i)$  is the diffuse or incoherent reflectance and  $\mathbf{R}(\mu) = \mathbf{R}(\mu, \mathbf{z}) + \delta \mathbf{R}(\mu)$  is the coherent or specular reflectivity. Note that  $\boldsymbol{\rho}_d$  and  $\delta \mathbf{R}$  are on the same order of magnitude, both being proportional to the wave height spectrum. Physically,  $\delta \mathbf{R}$  accounts for the reduction in the specular reflection due to diffuse scattering or diffraction effects, while  $\boldsymbol{\rho}_d$  describes the directional dependence of this scattered radiation.

## APPENDIX B

### POLARIZATION BASIS VECTORS

The horizontal and vertical polarization basis vectors in the global coordinate system are defined as

$$\mathbf{h} = (\mathbf{z} \times \mathbf{k})/|\mathbf{z} \times \mathbf{k}| = (\mathbf{z} \times \mathbf{k})/\sin \theta \\ \mathbf{v} = \mathbf{h} \times \mathbf{k} = (\mathbf{k} \cos \theta - \mathbf{z})/\sin \theta \quad (\text{B1})$$

where  $\mathbf{k}$  is the unit vector in the direction of observation and  $\theta = \cos^{-1}(\mathbf{k} \cdot \mathbf{z})$  is the global scattering angle. Since the  $\mathbf{z}'$  axis in the local coordinate system is equivalent to the local surface normal

$\mathbf{n}$ , the polarization basis vectors in this coordinate system can be written as

$$\begin{aligned}\mathbf{h}' &= (\mathbf{n} \times \mathbf{k})/|\mathbf{n} \times \mathbf{k}| = (\mathbf{n} \times \mathbf{k})/\sin \theta' \\ \mathbf{v}' &= \mathbf{h}' \times \mathbf{k} = (\mathbf{k} \cos \theta' - \mathbf{n})/\sin \theta'\end{aligned}\quad (\text{B2})$$

where  $\theta' = \cos^{-1}(\mathbf{k} \cdot \mathbf{n})$  is the local incidence angle. Since  $\mathbf{h}, \mathbf{v}, \mathbf{h}'$ , and  $\mathbf{v}'$  are all coplanar, the angle ( $\alpha$ ) between them is given by

$$\mathbf{h} \cdot \mathbf{h}' = \frac{(\mathbf{z} \times \mathbf{k}) \cdot (\mathbf{n} \times \mathbf{k})}{\sin \theta \sin \theta'} = \frac{n_z - k_z \cos \theta'}{\sin \theta \sin \theta'} = \cos \alpha \quad (\text{B3})$$

$$\mathbf{h} \cdot \mathbf{v}' = \frac{(\mathbf{z} \times \mathbf{k}) \cdot (\mathbf{k} \cos \theta' - \mathbf{n})}{\sin \theta \sin \theta'} = \frac{n_x k_y - n_y k_x}{\sin \theta \sin \theta'} = \sin \alpha \quad (\text{B4})$$

where  $n_x, n_y$ , and  $n_z$  are the components of  $\mathbf{n}$ , and  $k_x, k_y$ , and  $k_z$  are the components of  $\mathbf{k}$  in the global coordinate system. The expressions in Appendix A can be used to calculate the statistics of the scattered field  $\mathbf{E} = E_{h'}\mathbf{h}' + E_{v'}\mathbf{v}'$  in the local coordinate system. The components of this scattered field in the global coordinate system are

$$\begin{aligned}E_h &= \mathbf{E} \cdot \mathbf{h} = E_{h'} \cos \alpha + E_{v'} \sin \alpha \\ E_v &= \mathbf{E} \cdot \mathbf{v} = E_{v'} \cos \alpha - E_{h'} \sin \alpha.\end{aligned}\quad (\text{B5})$$

The statistics of the scattered field in the global coordinate system are then given by

$$\begin{aligned}\langle E_h E_h^* \rangle &= \langle E_{h'} E_{h'}^* \rangle \cos^2 \alpha + \langle E_{v'} E_{v'}^* \rangle \sin^2 \alpha \\ &\quad + 2\text{Re}\langle E_{h'} E_{v'}^* \rangle \sin \alpha \cos \alpha\end{aligned}\quad (\text{B6})$$

$$\begin{aligned}\langle E_v E_v^* \rangle &= \langle E_{v'} E_{v'}^* \rangle \cos^2 \alpha + \langle E_{h'} E_{h'}^* \rangle \sin^2 \alpha \\ &\quad - 2\text{Re}\langle E_{h'} E_{v'}^* \rangle \sin \alpha \cos \alpha\end{aligned}\quad (\text{B7})$$

$$\begin{aligned}\langle E_h E_v^* \rangle &= \langle E_{h'} E_{v'}^* \rangle \cos^2 \alpha - \langle E_{v'} E_{h'}^* \rangle \sin^2 \alpha \\ &\quad + \{ \langle E_{v'} E_{v'}^* \rangle - \langle E_{h'} E_{h'}^* \rangle \} \sin \alpha \cos \alpha.\end{aligned}\quad (\text{B8})$$

Using the definition of the modified Stokes vector in (2), the components of the bidirectional reflectance vector in the global coordinate system are then given by (14)–(17).

### APPENDIX C

#### APPARENT SLOPE PROBABILITY DISTRIBUTION

The surface slope probability density function  $p(\eta_x, \eta_y)$  for a random surface can be defined such that  $p(\eta_x, \eta_y)d\eta_x d\eta_y$  represents the probability that a ray passing vertically through the surface will encounter a slope in the range from  $\eta_x$  to  $\eta_x + d\eta_x$  in the  $x$  direction and from  $\eta_y$  to  $\eta_y + d\eta_y$  in the  $y$  direction. This probability is proportional to the vertically projected area of the surface elements having slopes in this interval, i.e.,

$$p(\eta_x, \eta_y)d\eta_x d\eta_y \propto (\mathbf{n} \cdot \mathbf{z})dA \quad (\text{C1})$$

where  $\mathbf{n}$  is the surface normal vector and  $dA$  is the total area of these surface elements. Similarly, the probability that a ray in the direction defined by the unit vector  $\mathbf{k}$  will encounter a slope in this interval is proportional to  $(\mathbf{n} \cdot \mathbf{k})dA$ . We therefore define the apparent slope probability density function  $p'(\eta_x, \eta_y)$  such that

$$p'(\eta_x, \eta_y)d\eta_x d\eta_y \propto (\mathbf{n} \cdot \mathbf{k})dA. \quad (\text{C2})$$

Eliminating  $dA$  from (C1) and (C2) yields

$$p'(\eta_x, \eta_y) \propto \frac{\mathbf{n} \cdot \mathbf{k}}{\mathbf{n} \cdot \mathbf{z}} p(\eta_x, \eta_y) \quad (\text{C3})$$

where the constant of proportionality is determined by the requirement that the apparent slope probability density function is normalized to unity. Using

$$\frac{\mathbf{n} \cdot \mathbf{k}}{\mathbf{n} \cdot \mathbf{z}} = k_z - \eta_x k_x - \eta_y k_y \quad (\text{C4})$$

and assuming the mean slope to be zero, the integral of the quantity on the right-hand side of (C3) over all slopes is equal to  $k_z = \mathbf{k} \cdot \mathbf{z}$ . Therefore, the apparent slope probability density function is equal to

$$p'(\eta_x, \eta_y) = \frac{(\mathbf{n} \cdot \mathbf{k})}{(\mathbf{n} \cdot \mathbf{z})(\mathbf{k} \cdot \mathbf{z})} p(\eta_x, \eta_y) \text{ for } \mathbf{n} \cdot \mathbf{k} > 0. \quad (\text{C5})$$

This pdf can also be written in terms of the surface normal vector instead of the surface slope. We define  $p_n(\mathbf{n})d\Omega_n$  as the probability that the surface normal lies within the solid angle  $d\Omega_n = \sin \theta_n d\theta_n d\phi_n$  where  $\theta_n$  and  $\phi_n$  are the polar and azimuthal angles of the normal vector, i.e.,

$$\mathbf{n} = (\sin \theta_n \cos \phi_n, \sin \theta_n \sin \phi_n, \cos \theta_n). \quad (\text{C6})$$

The surface slopes  $\eta_x$  and  $\eta_y$  are related to the components of the surface normal through the equations

$$\begin{aligned}\eta_x &= -n_x/n_z = -\tan \theta_n \cos \phi_n \\ \eta_y &= -n_y/n_z = -\tan \theta_n \sin \phi_n\end{aligned}\quad (\text{C7})$$

from which we obtain the Jacobian

$$\frac{\partial(\eta_x, \eta_y)}{\partial(\theta_n, \phi_n)} = \frac{\partial \eta_x}{\partial \theta_n} \frac{\partial \eta_y}{\partial \phi_n} - \frac{\partial \eta_x}{\partial \phi_n} \frac{\partial \eta_y}{\partial \theta_n} = \tan \theta_n \sec^2 \theta_n. \quad (\text{C8})$$

Equating  $p_n(\mathbf{n})d\Omega_n$  with  $p(\eta_x, \eta_y)d\eta_x d\eta_y$ , the probability density function for  $\mathbf{n}$  can therefore be written as

$$p_n(\mathbf{n}) = p(\eta_x, \eta_y) \sec^3 \theta_n = p(\eta_x, \eta_y)/n_z^3. \quad (\text{C9})$$

Following (C5), the probability that a ray in the direction  $\mathbf{k}$  will encounter a surface normal  $\mathbf{n}$  is given by

$$p'_n(\mathbf{n}) = \frac{\mathbf{n} \cdot \mathbf{k}}{n_z k_z} p_n(\mathbf{n}) = p(\eta_x, \eta_y) \frac{\cos \theta'}{\cos \theta} \sec^4 \theta_n \quad (\text{C10})$$

where  $\theta'$  is the local scattering angle and  $\theta$  is the global scattering angle corresponding to the vector  $\mathbf{k}$ .

### REFERENCES

- [1] P. W. Gaiser, K. M. St. Germaine, E. M. Twarog, G. A. Poe, W. Purdy, D. Richardson, W. Grossman, W. L. Jones, D. Spencer, G. Golba, J. Cleveland, L. Choy, R. M. Bevilacqua, and P. S. Chang, "The WindSat spaceborne polarimetric microwave radiometer: Sensor description and early orbit performance," *IEEE Trans. Geosci. Remote Sens.*, vol. 42, no. 11, pp. 2347–2361, Nov. 2004.
- [2] A. Stogryn, "The apparent temperature of the sea at microwave frequencies," *IEEE Trans. Antennas Propagat.*, vol. AP-15, pp. 278–286, Mar. 1967.
- [3] T. T. Wilheit, "A model for the microwave emissivity of the ocean's surface as a function of wind speed," *IEEE Trans. Geosci. Electron.*, vol. GE-17, pp. 244–249, Oct. 1979.

- [4] D. B. Kunkee, "Ocean surface foam modeling for passive remote sensing of ocean surface wind vectors," in *Proc. IGARSS*, vol. 5, 1998, pp. 2336–2338.
- [5] P. M. Smith, "The emissivity of sea foam at 19 and 37 GHz," *IEEE Trans. Geosci. Remote Sens.*, vol. 26, no. 5, pp. 541–547, Sep. 1988.
- [6] L. A. Rose, W. E. Asher, S. C. Reising, P. W. Gaiser, K. M. St. Germaine, D. J. Dowgiallo, K. A. Horgan, G. Farquharson, and E. J. Knapp, "Radiometric measurements of the microwave emissivity of foam," *IEEE Trans. Geosci. Remote Sens.*, vol. 40, no. 12, pp. 2619–2625, Dec. 2002.
- [7] E. Monahan and D. K. Woolf, "Comments on variations of whitecap coverage with wind stress and water temperature," *J. Phys. Oceanogr.*, vol. 19, no. 5, pp. 706–709, 1989.
- [8] F. J. Wentz, "A two-scale model for foam-free sea microwave brightness temperatures," *J. Geophys. Res.*, vol. 80, pp. 3441–3446, 1975.
- [9] S. H. Yueh, "Modeling of wind direction signals in polarimetric sea surface brightness temperatures," *IEEE Trans. Geosci. Remote Sens.*, vol. 35, no. 6, pp. 1400–1418, Nov. 1997.
- [10] K. St. Germain, G. A. Poe, and P. W. Gaiser, "Polarimetric emission model of the sea at microwave frequencies and comparison with measurements," *Progr. Electromagn. Res.*, vol. PIER-37, pp. 1–30, 2002.
- [11] D. R. Lyzenga and J. F. Vesecky, "Two-scale polarimetric emissivity model: Efficiency improvements and comparisons with data," *Progr. Electromagn. Res.*, vol. PIER-37, pp. 205–219, 2002.
- [12] V. G. Irisov, "Small-slope expansion for thermal and reflected radiation from a rough surface," *Waves Random Media*, vol. 7, pp. 1–10, 1997.
- [13] —, "Azimuthal variation of the microwave radiation from a slightly non-Gaussian sea surface," *Radio Sci.*, vol. 35, no. 1, pp. 65–82, Jan.–Feb. 2000.
- [14] J. T. Johnson and M. Zhang, "Theoretical study of the small slope approximation for ocean polarimetric thermal emission," *IEEE Trans. Geosci. Remote Sens.*, vol. 37, no. 5, pp. 2305–2316, Sep. 1999.
- [15] J. T. Johnson and Y. Cai, "A theoretical study of sea surface up/down wind brightness temperature differences," *IEEE Trans. Geosci. Remote Sens.*, vol. 40, no. 1, pp. 66–78, Jan. 2002.
- [16] J. T. Johnson, "Comparison of the physical optics and small slope theories for polarimetric thermal emission from the sea surface," *IEEE Trans. Geosci. Remote Sens.*, vol. 40, no. 2, pp. 500–504, Feb. 2002.
- [17] H. J. Liebe, G. A. Hufford, and M. G. Cotton, "Propagation modeling of moist air and suspended water/ice particles at frequencies below 1000 GHz," in *AGARD Conf. Proc. 542, Atmospheric Propagation Effects through Natural and Man-Made Obscurants for Visible to MM-Wave Radiation*, Berlin, Germany, May 1993.
- [18] P. J. Flatau, R. L. Walko, and W. R. Cotton, "Polynomial fits to saturation vapor pressure," *J. Appl. Meteorol.*, vol. 31, pp. 1507–1513, 1992.
- [19] F. J. Wentz and T. Meissner, "AMSR ocean algorithm Theoretical Basis Document Version 2," *Remote Sens. Syst.*, Santa Rosa, CA, Doc. 121599A-1, Nov. 2, 2000.
- [20] W. Ellison, A. Balana, G. Delbos, K. Lamkaouchi, L. Eymard, C. Guillou, and C. Prigent, "New permittivity measurements of seawater," *Radio Sci.*, vol. 33, no. 3, pp. 639–648, May–Jun. 1998.
- [21] C. Cox and W. Munk, "Measurement of the roughness of the sea surface from photographs of the sun's glitter," *J. Opt. Soc. Amer.*, vol. 44, pp. 838–850, 1954.
- [22] T. Hara and W. J. Plant, "Hydrodynamic modulation of short wind-wave spectra by long waves and its measurement using microwave backscatter," *J. Geophys. Res.*, vol. 99, pp. 9767–9784, 1994.
- [23] D. R. Lyzenga, "Ocean wave spectrum and dissipation rate derived from CMOD4 model function," *J. Geophys. Res.*, vol. 109, no. C7, C07019, 2004. DOI:10.1029/2003JC002237.
- [24] A. Stoffelen and D. Anderson, "Scatterometer data interpretation: Estimation and validation of the transfer function CMOD4," *J. Geophys. Res.*, vol. 102, pp. 5767–5780, 1997.
- [25] O. M. Phillips, "On the generation of waves by turbulent wind," *J. Fluid Mech.*, vol. 2, pp. 417–445, 1957.
- [26] W. J. Pierson and L. Moskowitz, "A proposed spectral form for fully developed seas based on the similarity theory of S. A. Kitaigorodskii," *J. Geophys. Res.*, vol. 69, pp. 5181–5190, 1964.
- [27] D. E. Hasselmann, M. Dunkel, and J. A. Ewing, "Directional wave spectra observed during JONSWAP 1973," *J. Phys. Oceanogr.*, vol. 10, pp. 1264–1280, 1980.
- [28] W. J. Plant, "A relationship between wind stress and wave slope," *J. Geophys. Res.*, vol. 87, pp. 1961–1967, 1982.
- [29] M. Perlin, H. Lin, and C.-L. Ting, "On parasitic capillary waves generated by steep gravity waves: An experimental investigation with spatial and temporal measurements," *J. Fluid Mech.*, vol. 255, pp. 597–620, 1993.
- [30] D. R. Lyzenga, "Effects of wave breaking on SAR signatures observed near the edge of the gulf stream," in *Proc. IGARSS*, vol. 2, 1996, pp. 906–910.
- [31] B. Jähne and K. Riemer, "Two-dimensional wave number spectra of small-scale water surface waves," *J. Geophys. Res.*, vol. 95, pp. 11 531–11 546, 1990.
- [32] J. Klinke and B. Jähne, "Two-dimensional wave number spectra of short wind waves: Results from wind-wave facilities and extrapolation to the ocean," in *SPIE Proc. Optics of the Air-Sea Interface: Theory and Measurement*, vol. 1749, 1992, pp. 245–257.
- [33] J. R. Apel, "An improved model of the ocean surface wave vector spectrum and its effects on radar backscatter," *J. Geophys. Res.*, vol. 99, pp. 16 269–16 291, 1994.
- [34] T. Elfouhaily, B. Chapron, K. Katsaros, and D. Vandemark, "A unified directional spectrum for long and short wind-driven waves," *J. Geophys. Res.*, vol. 102, pp. 15 781–15 796, 1997.
- [35] V. Kudryavtsev, D. Hauser, G. Caudal, and B. Chapron, "A semiempirical model of the normalized radar cross section of the sea surface 1. Background model," *J. Geophys. Res.*, vol. 108, no. C3, 8054, 2003. DOI: 10.1029/2001JC001003.
- [36] C. H. Dey and L. L. Morone, "Evolution of the national meteorological center global data assimilation system: January 1982–December 1983," *Mon. Weather Rev.*, vol. 113, pp. 304–318, 1985.
- [37] S. A. Tjemkes and M. Visser, "Horizontal variability of temperature, specific humidity, and cloud liquid water as derived from spaceborne observations," *J. Geophys. Res.*, vol. 99, pp. 23 089–23 105, 1994.
- [38] T. Meissner and F. J. Wentz, "An updated analysis of the ocean surface wind direction signal in passive microwave brightness temperatures," *IEEE Trans. Geosci. Remote Sens.*, vol. 40, no. 6, pp. 1230–1240, Jun. 2002.
- [39] F. J. Wentz, "Measurement of oceanic wind vector using satellite microwave radiometers," *IEEE Trans. Geosci. Remote Sens.*, vol. 30, no. 5, pp. 960–972, Sep. 1992.
- [40] S. H. Yueh, R. T. Shin, and J. A. Kong, "Scattering of electromagnetic waves from a periodic surface with random roughness," *J. Appl. Phys.*, vol. 64, pp. 1657–1670, 1988.



**David R. Lyzenga** received the B.S.E. degree in engineering physics from the University of Michigan, Ann Arbor, the M.S. degree in physics from Yale University, New Haven, CT, and the Ph.D. degree in electrical engineering from the University of Michigan, in 1967, 1968, and 1973, respectively.

He worked at the Environmental Research Institute of Michigan from 1974 to 1987, and was an Associate Professor in the College of Marine Studies, University of Delaware from 1987 to 1989. He presently holds joint research appointments at the University of Michigan and the General Dynamics Advanced Information Systems Division, Ann Arbor. His research interests include interactions of electromagnetic radiation with the ocean, and remote sensing of the ocean using both radar and optical techniques.